A5 Gravitational Waves - Coursework Report

Jacob Tutt (JLT67)

Department of Physics, University of Cambridge

June 19, 2025

Word Count: 2999

1 Introduction

Although predicted by Einstein in 1916, the first direct detection of gravitational waves (GWs) from the binary black hole merger GW150914 [1] wasn't achieved until a century later. However, such detections have become increasingly routine, with over 290 GW events [2] having been observed as of 19th March 2025. This work looks at some of the key statistical techniques used during GW analysis for rapid signal detection and sky localisation, which are essential for allowing follow-up observations to be made in the era of multi-messenger astronomy. First achieved for GW170817 [3], complementary electromagnetic (EM) observations allow phenomena such as kilonovae [4] to be studied for mergers involving neutron stars. Additionally, GWs serve as 'standard sirens' [5], offering an independent measurement of the distance–redshift relation, which can be used to constrain cosmological parameters.

2 Data

2.1 Interferometers

Modern interferometers use interference patterns to measure changes $\Delta L(t)$ in the distance traveled by lasers along two perpendicular arms of length L, caused by wave-like distortions in the geometry of space-time. This is quantified by the strain, $h(t)$:

$$h(t) = \frac{\Delta L(t)}{L} \tag{1}$$

The following work makes use of data provided by three laser interferometers: Hanford (H1), Livingston (L1), and Virgo (V1). The Hanford and Livingston detectors form the LIGO observatory [6] and have arms 4 km in length. As a result, they typically exhibit lower strain noise and thus achieve a higher signal-to-noise ratio (SNR) compared to Virgo, which has 3 km arms [7]. Consequently, H1 and L1 serve as the primary detectors in this analysis. This is evidenced by their systematically lower power spectral density ($S_n(f)$), as shown in Figure 1, a measure of the mean square noise fluctuations per frequency bin (assuming Gaussian, stationary noise):

$$\langle \tilde{n}(f)\tilde{n}^*(f') \rangle = \frac{1}{2} S_n(f)\delta(f - f') \tag{2}$$

That said, a detector's sensitivity to the GW's plus (h_+) and cross ($h_\times$) polarizations also depends on its geographic position and orientation relative to the source, quantified by the antenna patterns ($F_+/F_\times$). Consequently, Virgo's location in Italy offers complementary sky coverage, improving sensitivity to regions that both US-based detectors lack, as illustrated in Figure 2.

$$\tilde{h}_{\text{det}}(f) = F_+\tilde{h}_+(f) + F_\times\tilde{h}_\times(f) \tag{3}$$
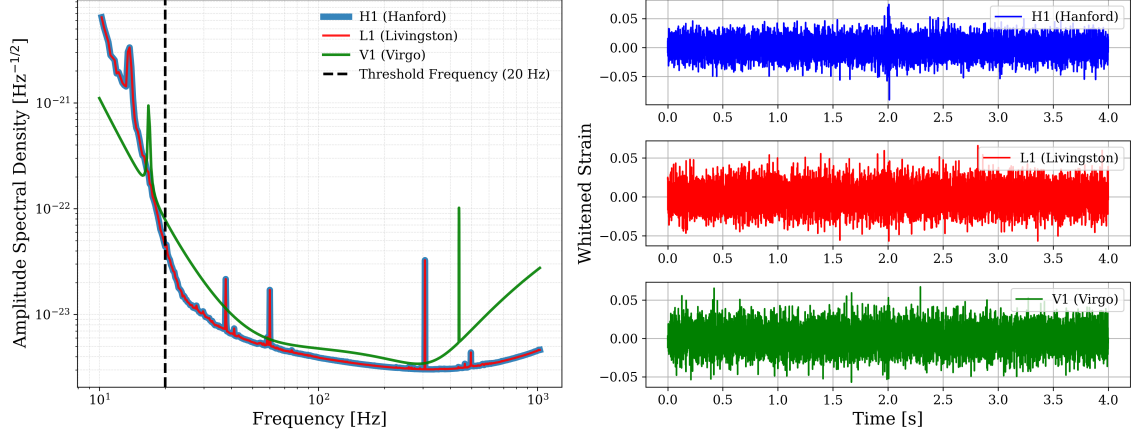
Figure 1: Amplitude Spectral Density and whitened strain data for each detector. Following common practise, values below 20 Hz are set to infinity.
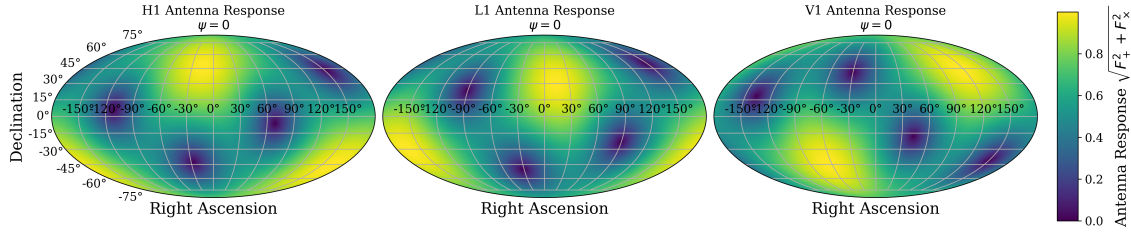

Figure 2: Antenna response functions for each detector at the GPS start time of the data

2.2 Waveform Model

During real-world GW analysis, the nature of the source and thus its true waveform is unknown. As a result, even for the simplest case of GWs emitted by a binary black hole (BBH) system in a circular orbit, a 15-dimensional parameter space is required to perform inference based on an interferometer's signal, $h(t, \boldsymbol{\theta}_{\mathrm{BBH}})$.

$$\boldsymbol{\theta}_{\mathrm{BBH}} = \{m_1, m_2, \vec{S}_1, \vec{S}_2, D_L, \alpha, \delta, \iota, \psi, t_c, \phi_c\} \tag{4}$$

- **Waveform parameters:** masses m_1, m_2, spin vectors $\vec{S}_1$, $\vec{S}_2$, inclination ι and coalescence phase ϕ_c.

- **Detection parameters:** luminosity distance D_L, right ascension α, declination δ, polarization angle ψ and time of coalescence t_c.

In the following analysis, we assume a fixed waveform model throughout, $h(t, \boldsymbol{\theta}_{\mathrm{Red}})$, displayed in Figure 3, and thus our parameter space is reduced to the five detection parameters, $\boldsymbol{\theta}_{\mathrm{Red}}$. The
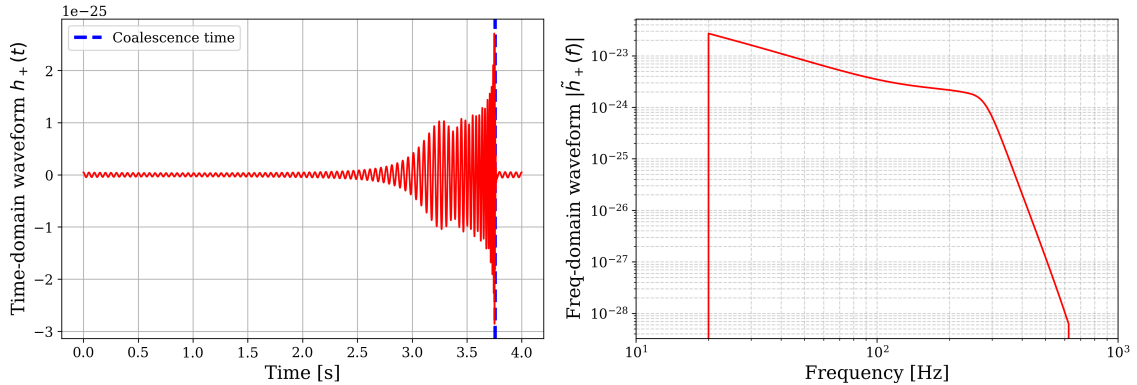

Figure 3: Fixed Waveform model in both time and frequency domain with a time from $t_c = 0 \rightarrow 3.75$ to aid visualisation.

time-domain waveform shows the inspiral, merger, and a rapid ringdown pattern characteristic of a GW.

$$\boldsymbol{\theta}_{\mathrm{Red}} = \{D_L, \alpha, \delta, \psi, t_c\} \tag{5}$$

3 Match Filtering

Matched filtering is a commonly employed signal processing technique for identifying gravitational wave events within the detector's noisy time series data. Although a detailed derivation of the methods is provided in `Notebook 0`, a brief overview is given below.

3.1 Mathematical Formulation

For a given waveform template, an 'optimal filter', $K(t)$, can be defined and cross-correlated with the interferometer output: $s(t) = n(t) + h(t)$, which contains both noise $n(t)$ and a potential event signal $h(t)$. This filter must be applied for all coalescence times t_c, effectively acting as a template that slides back and forth, forming a convolution:

$$\rho_{\mathrm{mf}}^2(t_c) = \frac{S^2}{N^2} = (S \star K)(t_c) = \int_{-\infty}^{\infty} dt\, S(t)K(t - t_c) \tag{6}$$

Using Parseval's theorem (Equation 7) and the translation property of the Fourier transform (Equation 8), this can be converted to the frequency domain:

$$\int_{-\infty}^{\infty} dt\, S(t)K^*(t) = \int_{-\infty}^{\infty} df\, \tilde{S}(f)\tilde{K}^*(f) \tag{7}$$

$$\mathcal{F}[K(t - t_c)](f) = \tilde{K}(f)e^{-2\pi i f t_c} \tag{8}$$

$$\rho_{\mathrm{mf}}^2(t_c) = \int_{-\infty}^{\infty} df\, \tilde{S}(f)\tilde{K}^*(f)e^{2\pi i f t_c} \tag{9}$$

Using the optimal filter which weights each frequency by the inverse of the spectral noise density (as proved in the repository) and the fact the time series is real.

$$\tilde{K}(f) = \frac{\tilde{h}(f)}{S_n(f)} \tag{10}$$

$$\rho_{\mathrm{mf}}^2(t_c) = \int_{-\infty}^{\infty} df\, \frac{\tilde{s}(f)\tilde{h}^*(f)}{S_n(f)}e^{2\pi i f t_c} \tag{11}$$

$$\rho_{\mathrm{mf}}^2(t_c) = 4\Re \int_{0}^{\infty} df\, \frac{\tilde{s}(f)\tilde{h}^*(f)}{S_n(f)}e^{2\pi i f t_c} \tag{12}$$

Finally by writing this an inverse Fourier transform:

$$\rho_{\mathrm{mf}}^2(t_c) = 4\Re \mathcal{F}^{-1}\left[\frac{\tilde{s}(f)\tilde{h}^*(f)}{S_n(f)}\right](t_c) \tag{13}$$

In practise, this was implemented on the discrete data using the inverse fast Fourier transform (IFFT).

3.2 Time Isolation Results

Although important to consider the Hanford and Livingston detectors independently from Virgo, due to the discussion provided in subsection 2.1, the results for each detector are presented together. Despite using a fixed waveform model, the interferometers' detections are not fixed due to their dependence on the antenna patterns (F_+ and $F_\times$), and thus on the source's RA, Dec, and ψ. These functions simply scale the plus and cross polarisations of the waveform and thus should not affect the inferred coalescence times t_c. However, they will directly affect the observed signal amplitude and thus the detection SNR.

To investigate this effect, matched filtering was performed using a set of antenna response functions generated from a mesh grid of evenly distributed RA, Dec, and ψ values, with 100, 50,

Table 1: Standard deviations of SNR and t_c across grid of RA, Dec, and ψ, with parameters that maximise the SNR for each detector.

Detector	$\sigma_{\mathbf{SNR}}$	σ_{t_c} (s)	RA (rad)	Dec (rad)	ψ (rad)
Hanford (H1)	5.329	0.001	0.381	0.796	1.988
Livingston (L1)	4.563	0.001	3.998	-0.535	2.885
Virgo (V1)	3.491	0.001	5.775	-0.739	2.372

Table 2: Maximum matched filter SNR and corresponding detection time.

Detector	Max SNR	Time (s)
Hanford (H1)	35.52	2.017 ± 0.002
Livingston (L1)	30.48	2.009 ± 0.002
Virgo (V1)	23.28	2.008 ± 0.002

and 50 samples respectively. The results of this optimisation are presented in Table 1, which show that there is negligible effect on the achieved t_c values over the grid, yet significant variation is seen across the SNR values. Despite this, we see no agreement between the 'optimal' sky coordinates and polarisations, highlighting the limitations of this approach and supporting the use of more advanced techniques such as triangulation and Bayesian inference throughout this work.

Using the 'optimal' matched filters from above, Table 2 and Figure 6 report the maximal SNR achieved for each detector alongside their corresponding coalescence times t_c and uncertainties, estimated via a simple full-width at half-maximum (FWHM) approximation. As expected, given the discussion in subsection 2.1, we find that the SNR achieved by Virgo is significantly lower than both Hanford (34.5%) and Livingston (23.62%).
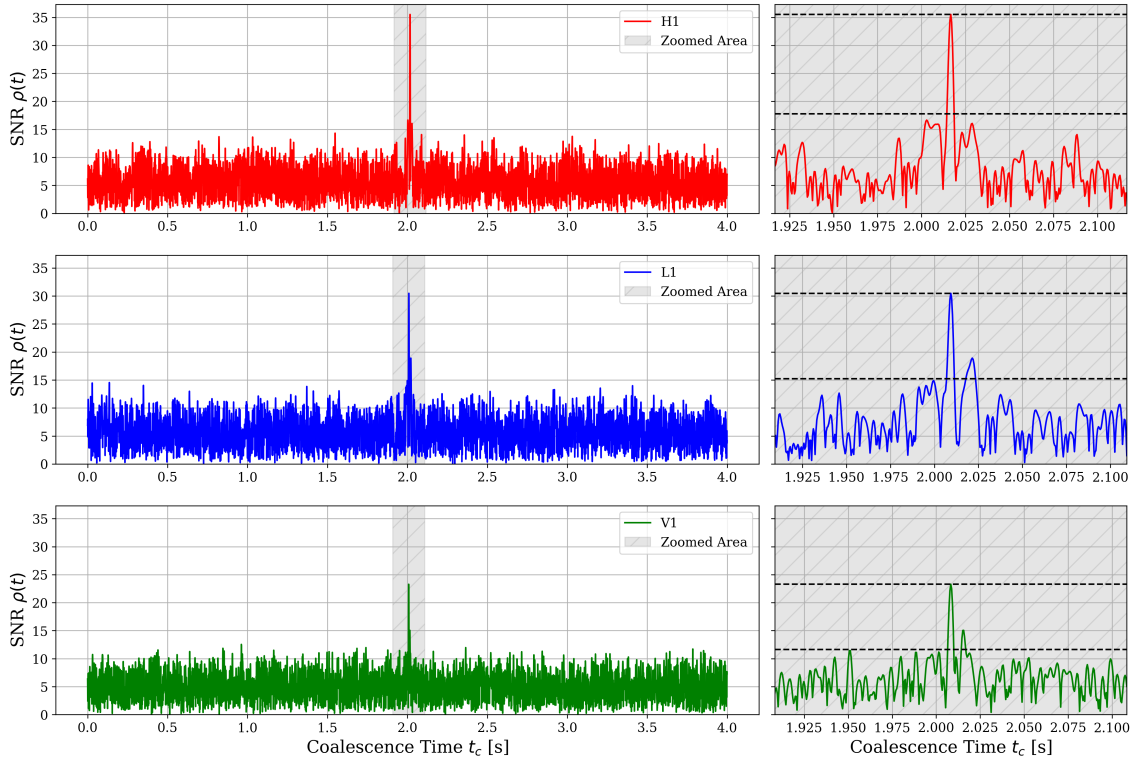

Figure 4: Matched filtering performed on strain data from the Hanford, Livingston, and Virgo detectors.

3.3 Sky Triangulation

Similarly to radio interferometry, the long baselines and the known propagation speed of GWs (speed of light, c), enable time delays between detectors to be used to constrain the source's location on the sky. Unlike electromagnetic waves, gravitational waves are not impeded by the Earth and hence can be detected from all directions (excluding sensitivity variations from the

Detector Pair	Time Delay (ms)	Total Light Travel Time (ms)
H1 - L1	7 ± 3	10
H1 - V1	8 ± 3	27
L1 - V1	0.1 ± 3.0	26

Table 3: Absolute Time Delays between Interferometers alongside the distant between detectors in light travel time for context.[9].

Detectors	1σ Area [deg^2] (% Sky)	2σ Area [deg^2] (% Sky)	3σ Area [deg^2] (% Sky)
H1 - L1	15671 (38.0)	20895 (50.7)	26468 (64.2)
H1 - V1	7144 (17.3)	12247 (29.7)	18075 (43.8)
L1 - V1	9857 (23.9)	15846 (38.4)	21378 (51.8)
H1 - L1 - V1	1611 (3.9)	3733 (9.1)	6339 (15.4)

Table 4: Confidence levels and sky areas for different detector log-likelihood combinations.

antenna pattern). This work exploits the `Bilby` package [8], which stores the precise position and orientation for each detector. Using these, the `time_delay_from_geocenter` function computes the expected time delay from the Earth's geocenter to a detector as a function of source sky position, $\tau_i(\alpha, \delta)$. For any pair of detectors, the theoretical time delay between detectors is given by:

$$\Delta t_{1,2}^{\text{true}}(\alpha, \delta) = \tau_1(\alpha, \delta) - \tau_2(\alpha, \delta). \tag{14}$$

These theoretical time delays can then be compared to the observed delays between detectors, defined as $\Delta t_{1,2}^{\text{obs}} = t_1 - t_2$, as presented in Table 3. To determine confidence intervals, we use a gaussian timing likelihood for each detector, which means that for a given pair of detectors:

$$\log \mathcal{L}_{1,2}(\alpha, \delta) \propto -\frac{1}{2} \left(\frac{\Delta t_{1,2}^{\text{obs}} - \Delta t_{1,2}^{\text{true}}(\alpha, \delta)}{\sigma_{1,2}} \right)^2 \tag{15}$$

And thus for more than two detectors, the likelihood across all baselines can be summed using:

$$\log \mathcal{L}(\alpha, \delta) \propto -\frac{1}{2} \sum_{i<j} \left(\frac{\Delta t_{i,j}^{\text{obs}} - \Delta t_{i,j}^{\text{true}}(\alpha, \delta)}{\sigma_{i,j}} \right)^2 \tag{16}$$

The log-likelihood values were calculated across the sky using a grid of RA and Dec Values. Given the assumption of normal distributed errors, the log-likelihood ratio statistic defined in Equation 17 will follow a Chi-Squared χ^2 Distribution with 2 degrees of freedom, in line with Wilk's Theorem. Confidence contours could therefore be drawn using the cumulative density thresholds of the χ^2 distribution. These contours are presented on sky maps in Figure 5 for each combination of detectors. Table 4 presents estimates of the sky area contained within each contour which were calculated using equal area Healpy pixels [10] (`nside = 16` $\rightarrow$ `npix = 3072`).

$$\Lambda = -2 \log \left(\frac{\mathcal{L}(\alpha, \delta)}{\mathcal{L}(\alpha, \delta)_{max}} \right) \tag{17}$$

We begin by discussing the results obtained using only the L1 and H1 detectors independently. Using just two detectors only provides a single baseline (generalised for N detectors in Equation 18), resulting in weak sky localisation power. In this case, we are only able to constrain the source's location to 38.0% of the sky with 68% (1σ) confidence. Such a broad area is completely infeasible for enabling follow-up EM observations in multi-messenger astronomy or, of more relevance to this work, host galaxy identification. We note that this sky area could be reduced by decreasing the uncertainty in our timing measurements, which are likely conservatively estimated in our analysis.

$$\text{No. Baselines} = \binom{N}{2} = \frac{N(N-1)}{2} \tag{18}$$

With the inclusion of the Virgo interferometer (V1), three independent baselines can be created, significantly increasing our ability to localise a source. Interestingly, even when considering the individual time delays involving Virgo, namely H1–V1 and L1–V1, they both provide substantially smaller areas than those from H1-L1. This improvement is a result of Virgo's location in
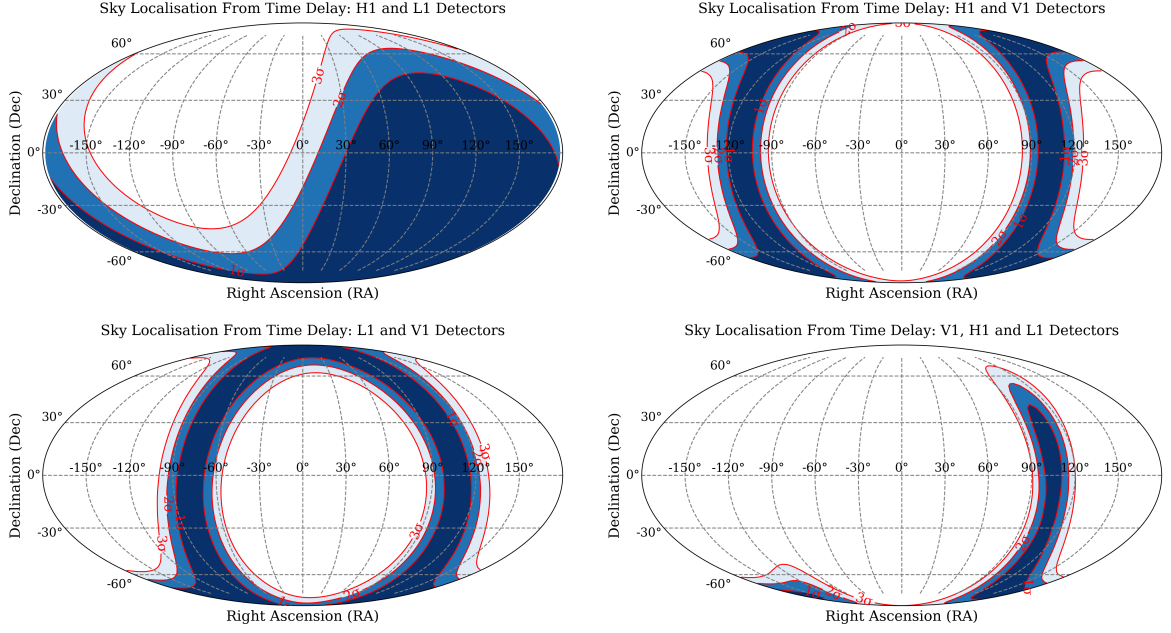
Figure 5: Sky maps showing the 1σ, 2σ, and 3σ confidence contours of source triangulation using time delays.

Europe providing longer baselines with the U.S.-based detectors. This is supported by the inverse correlation between the sky localisation area (Table 4) and the baseline length [9] (Table 3).

Finally, when considering all three baselines together (Equation 16), we are able to isolate an area on the sky of 1611 deg^2 (3.9%) with 68% confidence. This marks an 89.7% decrease from the results provided using just the H1 and L1 detectors. Although still too large to provide an estimate of an exact host galaxy, this could be further reduced by decreasing the timing uncertainties or incorporating additional detectors such as KAGRA [11], GEO600 [12], or the upcoming LIGO-India [13].

4 Bayesian Inference

In the following section, we apply a Bayesian methodology to explore the posterior distribution of the five-dimensional 'observational' parameter space outlined in subsection 2.2.

4.1 Likelihood

We first outline the formulation of the likelihood function this analysis employs, the basis of which assumes that the noise in the time domain is stationary and Gaussian. Consequently, under a noise-only model H_{noise}, the likelihood can be formulated as:

$$\mathcal{L}(n \mid H_{\text{noise}}) = \prod_{i=0}^{N} \mathcal{L}(\tilde{n}(f_i) \mid H_{\text{noise}}) = \mathcal{N} \exp\left(-\frac{(n|n)}{2}\right) \tag{19}$$

where the inner product is defined using the PSD $S_n(f)$ given in Equation 2:

$$(a|b) = 4\,\Re\left[\int_0^\infty df\, \frac{\tilde{a}(f)\tilde{b}^*(f)}{S_n(f)}\right] = 4\,\Delta f\,\Re\left[\sum_{i=0}^{N_f-1} \frac{\tilde{a}(f)\tilde{b}^*(f)}{S_n(f)}\right] \tag{20}$$

Thus assuming a signal is present with a detector response $h_{\vec{\theta}}(t)$ the likelihood can be written as:

$$\mathcal{L}(d, \vec{\theta}) = \mathcal{P}(d \mid \vec{\theta}, H_{\text{signal}}) = \mathcal{P}(d - h_{\vec{\theta}} \mid H_{\text{noise}}) \tag{21}$$

$$\mathcal{L}(d, \vec{\theta}) = \mathcal{N} \exp\left(-\frac{\langle d - h_{\vec{\theta}} | d - h_{\vec{\theta}} \rangle}{2}\right) = \mathcal{N} \exp\left(-\frac{1}{2}\, 4\,\Delta f \sum_{i=0}^{N} \frac{|\tilde{d}(f_i) - \tilde{h}_{\vec{\theta}}(f_i)|^2}{S_n(f_i)}\right) \tag{22}$$

6

$$\log \mathcal{L}(d \mid \vec{\theta}) \propto -2\,\Delta f \sum_{i=0}^{N_f-1} \frac{|\tilde{d}(f_i) - \tilde{h}_{\vec{\theta}}(f_i)|^2}{S_n(f_i)} \tag{23}$$

The formulation above assumes a single detector, however can be generalised for multiple detectors, $\{d_{\mathcal{I}}\}_{\mathcal{I}=1}^{N_{\det}}$ as such:

$$\mathcal{P}(\{d_{\mathcal{I}}\} \mid \vec{\theta}) = \prod_{\mathcal{I}} \mathcal{P}(d_{\mathcal{I}} \mid \vec{\theta}) \propto \exp\left(-\sum_{\mathcal{I}} \frac{\langle d_{\mathcal{I}} - h_{\vec{\theta}} \mid d_{\mathcal{I}} - h_{\vec{\theta}} \rangle}{2}\right) \tag{24}$$

$$\log \mathcal{L}(\{d_{\mathcal{I}}\} \mid \vec{\theta}) \propto -2\Delta f \sum_{\mathcal{I}=1}^{N_{\det}} \sum_{i=0}^{N_f-1} \frac{|\tilde{d}_{\mathcal{I}}(f_i) - \tilde{h}_{\vec{\theta},\mathcal{I}}(f_i)|^2}{S_n^{(\mathcal{I})}(f_i)} \tag{25}$$

For a fixed waveform (Figure 3), we must account for the parameters RA, Dec, ψ, D_l, and t_c^{geo}. The first of these are accounted for by each detector's antenna patterns, as previously discussed. For $F_\times$ and F_+, we assume that time can be treated as constant at the GPS start time, as its variation has a negligible effect over the 4-second signal.

$$\tilde{h}_{\det}(f) = F_+(RA, Dec, \psi)\,\tilde{h}_+(f) + F_\times(RA, Dec, \psi)\,\tilde{h}_\times(f) \tag{26}$$

To ensure a consistent definition of time, all detector waveforms are defined relative to the time of coalescence at the Earth's geocenter, t_c^{geo}. The corresponding time delays to each detector are then applied prior to performing the Fourier transform:

$$t_c^{\text{detector}} = t_c^{\text{geo}} + t_{\text{delay}}^{\text{detector}}(\text{Ra, Dec}) \tag{27}$$

$$h_{\det}(t_c^{\text{geo}}) \xrightarrow{\mathcal{F}} \tilde{h}_{\det} e^{2\pi i f t_c^{\text{detector}}} \tag{28}$$

Finally, the effect of the luminosity distance D_L is incorporated through its inverse proportionality to the observed gravitational wave amplitude:

$$\tilde{h}_{\det}(f; D_L) = \left(\frac{1\text{Gpc}}{D_L}\right) \tilde{h}_{\det}(f) \tag{29}$$
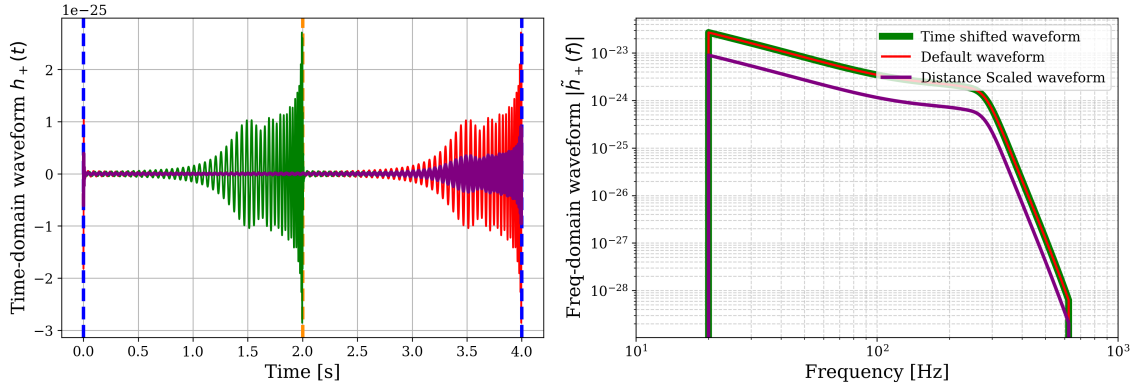

Figure 6: The effects of scaling (D_l) and shifting (t_c^{geo}) on the waveform's time and frequency domains.

4.2 Priors

The priors presented in Table 5 were chosen to be uninformative to provide an unbiased analysis and thereby allow a direct and fair comparison of results presented in section 3. While the uniform priors for right ascension, polarization angle (ψ), and the coalescence time at the geocenter (t_{geo}^c) are straightforward, we provide further justification for the choices made for the luminosity distance D_l and declination. To remain uninformative about the source's position on the celestial sphere, the prior must assign equal probability per unit area on the sky. This requires accounting for the geometric convergence near the celestial poles at $\text{Dec} = \pm\frac{\pi}{2}$. To achieve this, we sample $\sin(\text{Dec})$ uniformly over the interval $[-1, 1]$. Secondly, we use a Jeffreys prior on the luminosity distance to allow scale invariance and better reflect the lack of knowledge of its order of magnitude.

Parameter	Prior Description
RA	Uniform over $[0, 2\pi]$
Dec	Uniform in solid angle: $\sin(\text{Dec}) \in [-1, 1]$
$\boldsymbol{\psi}$	Uniform over $[0, \pi]$
$\boldsymbol{t^c_{\text{geo}}}$	Uniform over $[0, 4]$ seconds
$\boldsymbol{D_l}$	Log-uniform over $[10^{-2}, 100]$ Gpc (i.e. 10 Mpc to 100 Gpc)

Table 5: Prior distributions of waveform parameters.

4.3 Nested Sampling

This work employed the `dynesty` nested sampling package [14] to perform stochastic sampling from the posterior, defined by the likelihood function and prior distribution derived earlier. Dynesty offers multiple nested sampling strategies through configurable parameters such as `bound`, which controls how the sampling region is defined and `sample`, which dictates how new live points are drawn.

Depending on the complexity of the posterior, these parameters can significantly affect the computational efficiency of the sampling. As a result, an initial optimisation was run using 500 live points and a `dlogz` of 0.1 to compare the runtimes and sampling efficiency over a grid of parameters. While the full results are provided in the associated repository, it was found that using multiple bounding ellipsoids (`bound='multi'`) and a random walk sampler (`sample='rwalk'`) was optimal. Given this, complete posterior runs were made using 3000 live points and a termination condition of `dlogz = 0.01`.

These analyses were performed for two likelihood configurations: firstly, using only the data from the Hanford (H1) and Livingston (L1) detectors, and secondly, incorporating the Virgo (V1) detector to leverage all three interferometers. The main results from both configurations are presented below. Full corner plots showing the posterior distributions for all five parameters in each case are provided in section 6 (Figure 11 and Figure 12). Additionally, Figure 13 presents a comparison of the convergence and resulting parameter distributions from the nested sampling runs.

4.4 Tabulated Results

The first notable observation when comparing the two posterior distributions is that all parameter estimates remain consistent between the two approaches. This is evidenced by every median value reported in Table 7 falling within the 68% (1σ) credible interval presented in Table 6. Additionally, when incorporating data from all three detectors, far better parameter constraints are achieved, with a $\sim$74% reduction in all parameter uncertainties presented in Table 7. Finally, once the expected time delay has been accounted for, the estimates of $t_c^{(\text{geo})}$ align with those presented in section 3, further validating the Bayesian approach.

4.5 Sky Localisation

Figure 7 shows the posterior sample distributions projected onto sky maps, with the corresponding time-delay confidence regions from section 3 shown for reference. The comparison shows that the Bayesian posteriors are entirely consistent with the results from section 3, but significantly more constrained. This improvement was quantified using HEALPix pixels and KDE density thresholds to calculate the sky area contained within each confidence contour, as presented in Table 8. Using

Parameter	Median	68%	90%	99%
RA	2.4561	$+0.1419$ -0.2692	$+0.1833$ -0.5199	$+0.2170$ -1.0819
Dec	-1.1364	$+0.1327$ -0.0935	$+0.2132$ -0.1239	$+0.3185$ -0.1472
ψ	2.5380	$+0.2903$ -0.1796	$+0.5443$ -0.2505	$+1.0975$ -0.3232
$t_c^{(\text{geo})}$	1.9997	$+0.0013$ -0.0007	$+0.0023$ -0.0010	$+0.0050$ -0.0012
D_L	1.0354	$+0.0474$ -0.0539	$+0.0789$ -0.0964	$+0.1247$ -0.1985

Table 6: Posterior estimates and credible intervals from the H1 and L1 detectors.

Parameter	Median	68%	90%	99%
RA	2.3217	$+0.0261$ -0.0251	$+0.0441$ -0.0414	$+0.0693$ -0.0650
Dec	-1.1952	$+0.0103$ -0.0101	$+0.0173$ -0.0167	$+0.0273$ -0.0256
ψ	2.6797	$+0.0364$ -0.0371	$+0.0601$ -0.0623	$+0.0950$ -0.0963
$t_c^{(\text{geo})}$	2.0004	$+0.0002$ -0.0002	$+0.0003$ -0.0003	$+0.0005$ -0.0004
D_L	1.0144	$+0.0345$ -0.0333	$+0.0602$ -0.0536	$+0.0973$ -0.0812

Table 7: Posterior estimates and credible intervals from the H1, L1, and V1 detectors.

Detectors	1σ Area [deg^2] (% Sky)	2σ Area [deg^2] (% Sky)	3σ Area [deg^2] (% Sky)
H1 - L1	60.43 (0.15)	168.70 (0.41)	334.04 (0.81)
H1 - L1 - V1	0.00 (0.00)	4.20 (0.01)	7.55 (0.02)

Table 8: Sky localization areas at the 1, 2, and 3σ confidence levels of the posterior samples from the H1–L1 and H1–L1–V1 detector likelihoods.

only the H1 and L1 detectors, the Bayesian method isolates just 0.15% of the sky with 68% confidence, down from 38% using the single-baseline time-delay approach. When incorporating all three detectors (H1, L1, and V1), the posterior becomes so tightly constrained ($\sim 1\,\text{deg}^2$ / 0.002% of the sky) that, even using a HEALPix resolution of `nside = 64` (49,152 pixels), we are unable to identify a pixel entirely within the contour. This is contrasted with the 1σ region of 1611 deg^2 obtained using all three time delays in section 3, over three orders of magnitude larger. Overall, the Bayesian approach provides significantly better localisation than simple triangulation, greatly increasing the chances of accurate host galaxy identification and subsequent cosmological inference.
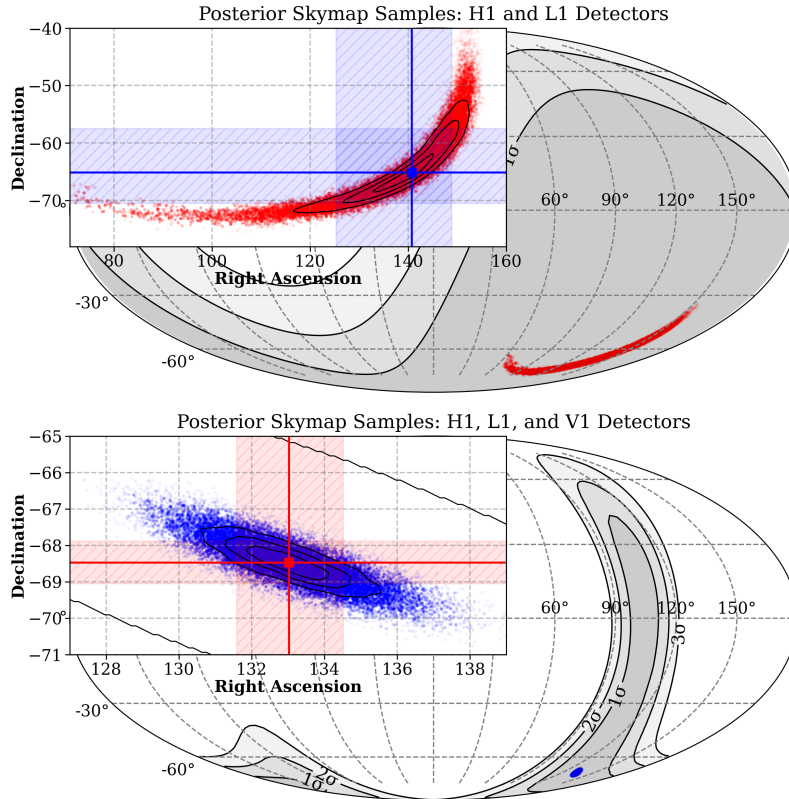

Figure 7: Comparison of posterior sample distributions on the sky (RA, Dec) for the H1–L1 and H1–L1–V1 detector configurations.

9

4.6 Luminosity Distance, D_L

Figure 8 and Table 7 show a similar trend in the posterior distribution of the luminosity distance, D_L, across the two analyses. The inclusion of an additional interferometer (Virgo) allows a tighter constraint on D_L and also shifts the median estimate closer to the true value of 1 Gpc. In downstream analysis, this enables greater accuracy in the inferred distance scale and, consequently, allows cosmological parameters to be inferred more precisely in section 5.
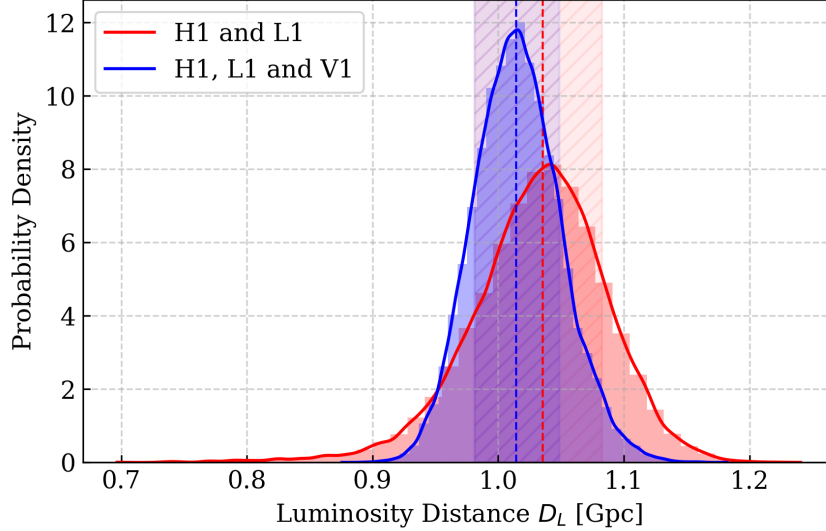

Figure 8: The luminosity distance, D_L, distribution for the H1–L1 and H1–L1–V1 detector posteriors.

5 Cosmological Inference

The following section explores the use of gravitational waves as 'standard sirens'. It focuses on the idea that by identifying the GW event's host galaxy, the distance–redshift relation can be determined and hence Hubble's constant H_0 inferred.

5.1 Host Galaxy Identification

The 90% confidence regions for both posterior estimates were determined using credible thresholds from a kernel density estimation (KDE) over a grid of right ascension (RA) and declination (Dec) values. As shown in Figure 9, for both the two-detector (H1–L1) and three-detector (H1–L1–V1) configurations, only a single galaxy (MGC+JN7U119) lies within their respective 90% confidence region. However, we still note that the three-detector posterior (right) provides a much stronger isolation of this host galaxy, with even its 100% confidence contour isolating MGC+JN7U119. In contrast, for the two-detector posterior (left), three additional galaxies lie marginally outside the 90% contour but all fall within the 96.5% confidence region. These galaxies are listed in Table 9.

Name	RA	Dec	Redshift, z
MGC+JN7U119	2.375	-1.211	0.226
MGC+JGS5HZS	2.543	-0.969	0.797
MGC+J07PCIH	2.706	-0.922	1.514
MGC+J2DG22T	1.993	-1.219	1.807

Table 9: Galaxies within the H1–L1 posterior's 96.5% confidence contour.

5.2 Hubble's Constant

Assuming the host galaxy to be MGC+JN7U119, as identified in subsection 5.1, the GW source can be concluded to be at a redshift, z, of 0.226. In the following analysis, we use Hubble's law (Equation 30) to relate the luminosity distance, D_L, with redshift, z. Furthermore, given the lack
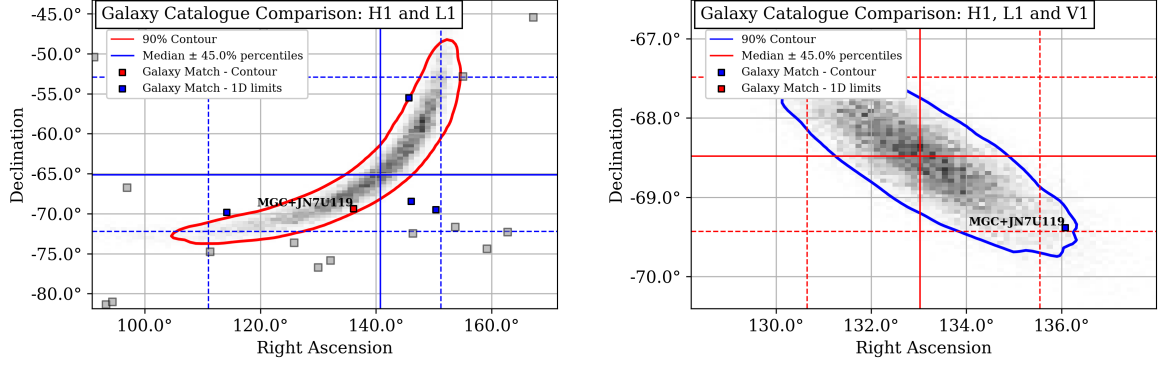
Figure 9: The 90% confidence contours of the posterior distributions for the H1–L1 and H1–L1–V1 detector configurations alongside the galaxy catalog.

of correlation between D_L and the spatial parameters (RA and Dec), as shown in Figure 12, it was not considered necessary to condition the posterior of D_L on the position of MGC+JN7U119 or to rerun the sampling in a reduced three-dimensional parameter space.

$$H_0 = \frac{c \cdot z}{D_L} \tag{30}$$

It is important to caveat this linear approximation, as it is only valid for low redshifts ($z \ll 1$). For larger redshifts, a more detailed expansion of the co-moving distance, r_{CM}, incorporating the changing expansion rate $H(z)$, is typically employed.

$$D_L = (1 + z)\, S_k[r_{CM}] \quad r_{CM} = c \int_0^z \frac{1}{H(z')} dz' \tag{31}$$

For a flat universe, $S_k[r_{CM}] = r_{CM}$. A second-order Taylor expansion (Equation 32) includes the deceleration parameter, q_0, which incorporates the matter density $\Omega_{M,0}$ and dark energy density $\Omega_{\Lambda,0}$ [15].

$$D_L \approx \frac{c}{H_0} \left[z + \frac{1}{2}(1 - q_0)z^2 + \cdots \right], \quad q_0 = \frac{1}{2}\Omega_{M,0} - \Omega_{\Lambda,0} \tag{32}$$

Using the samples from the three-detector posterior and Equation 30, we obtain an estimate for the Hubble constant of $H_0 = 66.79^{+2.19}_{-2.27}$ km/s/Mpc. There has long been reported statistical tension between the estimated Hubble constants determined through early-Universe surveys, such as the Cosmic Microwave Background (CMB), and late-Universe observations. This is outlined in Table 10. Our gravitational wave based estimate shows consistency with estimates provided by the Planck CMB results [16], with its reported value of $H_0 = 67.4$ falling within our 1σ uncertainty
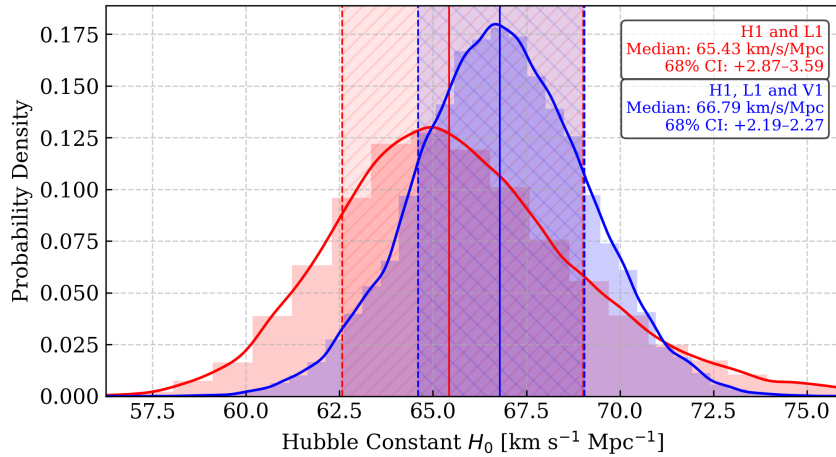

Figure 10: The distribution of the Hubble Constant for both posterior samples assuming MGC+JN7U119 as host galaxy.

Method	H_0 [km/s/Mpc]
Distance ladder (Milky Way Cepheids)	73.2 ± 1.3
H0LiCOW Gravitational lensing	73.3 ± 1.7
Planck CMB	67.4 ± 0.5

Table 10: Hubble constant H_0 measurments from different surveys illustrating statistical tensions [17, 16, 18].

window. However, it does not strongly align with the higher values reported by the local distance ladder from the Milky Way Cepheids [17] and gravitationally lensed quasars [18].
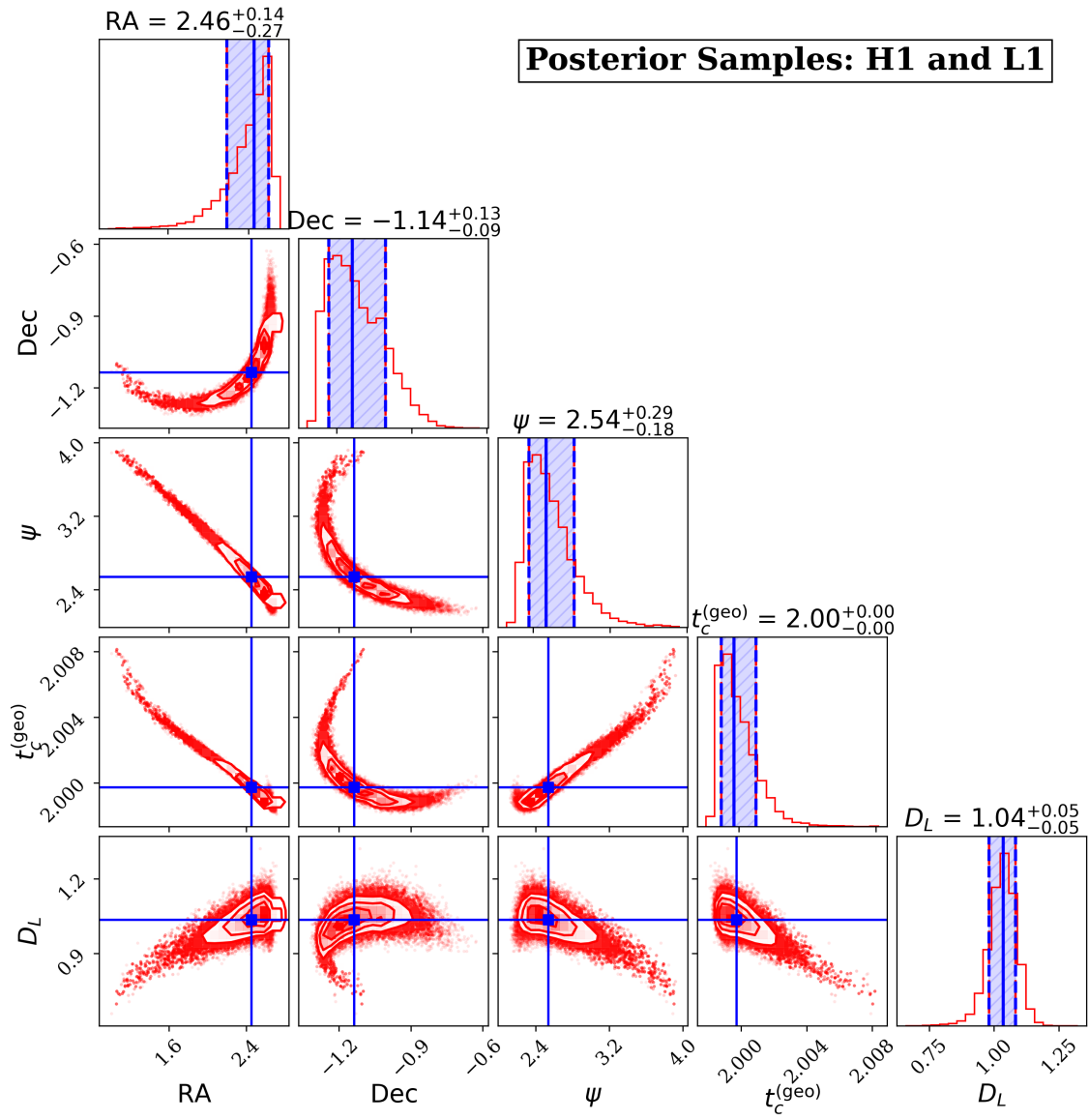
6   Additional Figures

Figure 11: Corner plot of posterior distributions from the H1 and L1 detectors.
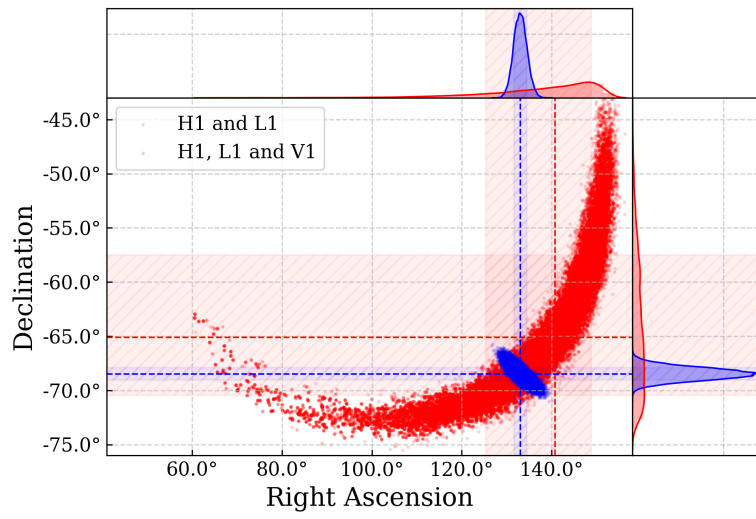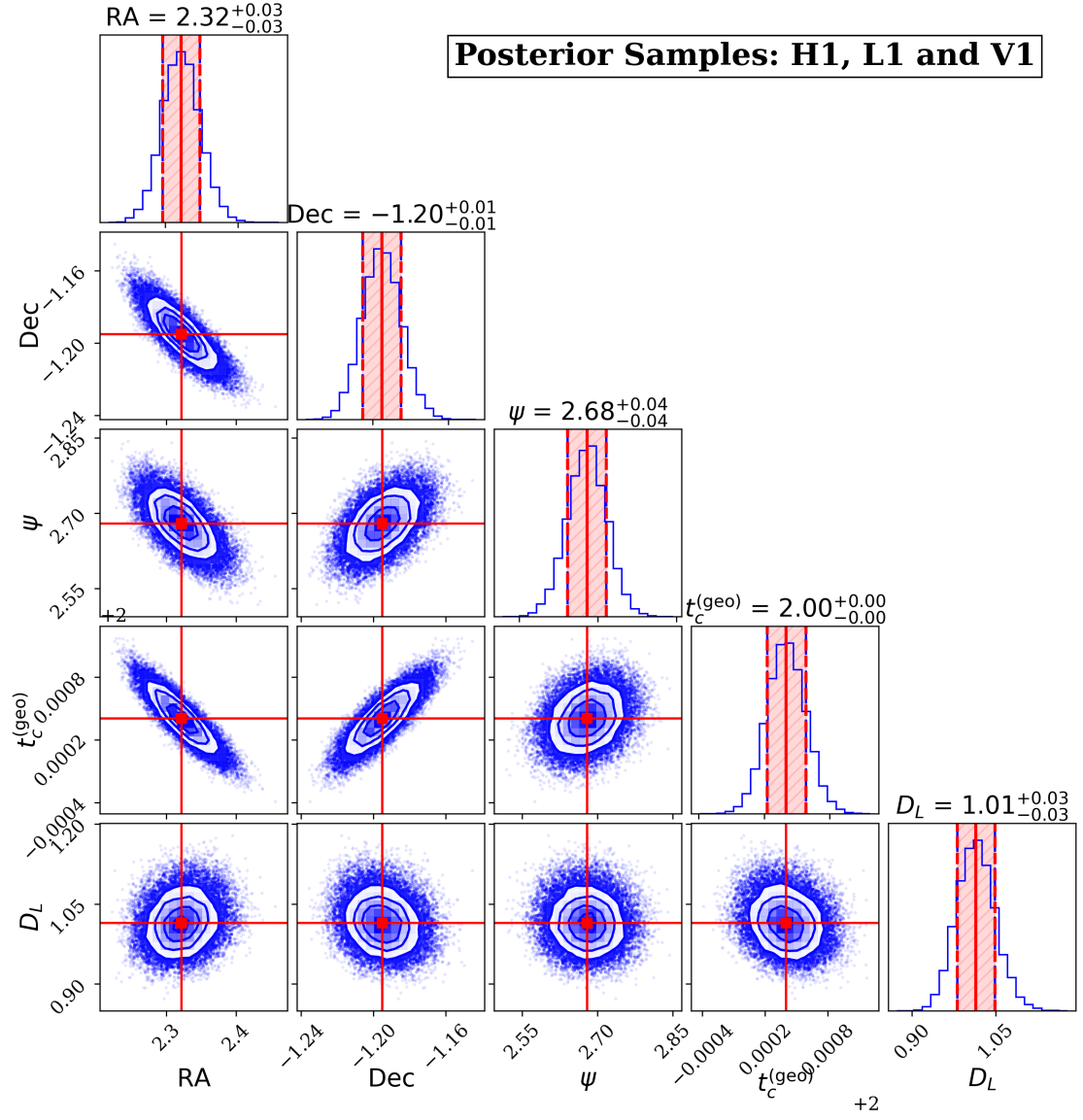
Figure 12: Top: Corner plot of posterior distributions from the H1, L1 and V1 detectors. Bottom: Comparison of RA and Dec posterior distributions between the H1–L1 and H1–L1–V1 detector configurations.
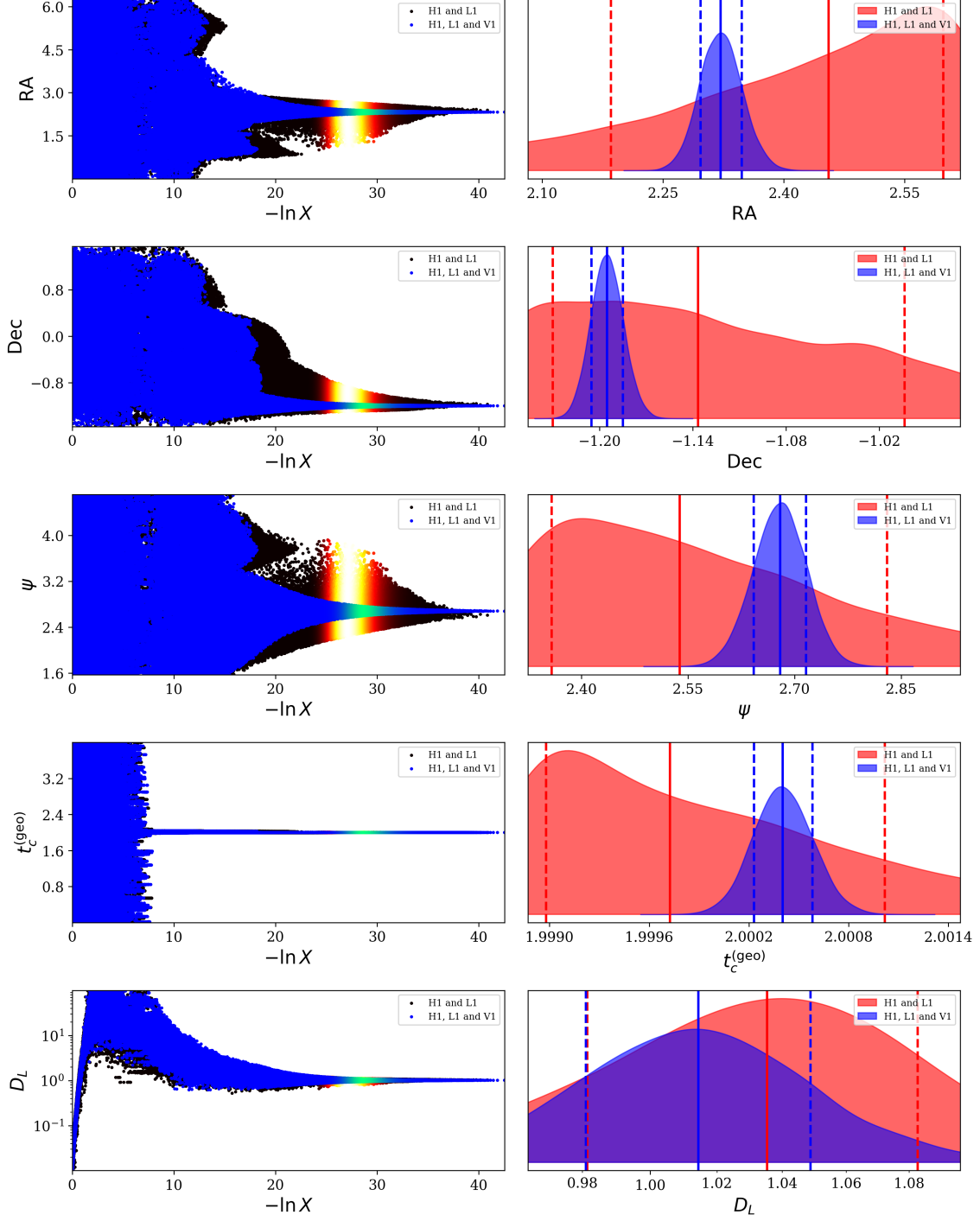
Figure 13: Convergence plot and posterior distributions of nested sampling runs for both the (H1-L1) and (H1-L1-V1) detector networks.

7 Declaration of Use of Autogeneration Tools

This report made use of Large Language Models (LLMs), to assist in the development of the project. These tools have been employed for assisting:

- Formatting plots to enhance presentation quality.
- Generating docstrings for the repository's documentation.
- Performing iterative changes to already defined code.
- Debugging code and identifying issues in implementation.
- Latex formatting for the report.
- Identifying spelling and punctuation inconsistencies within the report.
- Suggesting more concise phrasing to reduce the word count.

References

[1] B. P. Abbott et al. "Observation of Gravitational Waves from a Binary Black Hole Merger". In: *Physical Review Letters* 116.6 (Feb. 2016). ISSN: 1079-7114. DOI: 10.1103/physrevlett.116.061102. URL: http://dx.doi.org/10.1103/PhysRevLett.116.061102.

[2] Kimberly Burtnyk. *LIGO–Virgo–KAGRA Announce the 200th Gravitational Wave Detection of O4!* LIGO Laboratory News Release, with contributions from the LVK communications team. Mar. 2025. URL: https://www.ligo.caltech.edu/news/ligo20250320.

[3] B. P. Abbott et al. "GW170817: Observation of Gravitational Waves from a Binary Neutron Star Inspiral". In: *Physical Review Letters* 119.16 (Oct. 2017). ISSN: 1079-7114. DOI: 10.1103/physrevlett.119.161101. URL: http://dx.doi.org/10.1103/PhysRevLett.119.161101.

[4] Brian D. Metzger. "Kilonovae". In: *Living Reviews in Relativity* 23.1 (Dec. 2019). ISSN: 1433-8351. DOI: 10.1007/s41114-019-0024-0. URL: http://dx.doi.org/10.1007/s41114-019-0024-0.

[5] Daniel E. Holz and Scott A. Hughes. "Using Gravitational-Wave Standard Sirens". In: *The Astrophysical Journal* 629.1 (Aug. 2005), pp. 15–22. ISSN: 1538-4357. DOI: 10.1086/431341. URL: http://dx.doi.org/10.1086/431341.

[6] J Aasi et al. "Advanced LIGO". In: *Classical and Quantum Gravity* 32.7 (Mar. 2015), p. 074001. ISSN: 1361-6382. DOI: 10.1088/0264-9381/32/7/074001. URL: http://dx.doi.org/10.1088/0264-9381/32/7/074001.

[7] F Acernese et al. "Advanced Virgo: a second-generation interferometric gravitational wave detector". In: *Classical and Quantum Gravity* 32.2 (Dec. 2014), p. 024001. ISSN: 1361-6382. DOI: 10.1088/0264-9381/32/2/024001. URL: http://dx.doi.org/10.1088/0264-9381/32/2/024001.

[8] Gregory Ashton et al. "BILBY: A user-friendly Bayesian inference library for gravitational-wave astronomy". In: *Astrophys. J. Suppl.* 241.2 (2019), p. 27. DOI: 10.3847/1538-4365/ab06fc. arXiv: 1811.02042 [astro-ph.IM].

[9] Michał Bejger. *Gravitational Waves – Lecture 4: Detectors.* https://users.camk.edu.pl/bejger/gw-lecture2020/4_detectors.pdf. Accessed: 2025-06-10. 2020.

[10] K. M. Gorski et al. "HEALPix: A Framework for High-Resolution Discretization and Fast Analysis of Data Distributed on the Sphere". In: *The Astrophysical Journal* 622.2 (Apr. 2005), pp. 759–771. ISSN: 1538-4357. DOI: 10.1086/427976. URL: http://dx.doi.org/10.1086/427976.

[11] T. Akutsu et al. "KAGRA: 2.5 generation interferometric gravitational wave detector". In: *Nature Astronomy* 3.1 (Jan. 2019), pp. 35–40. ISSN: 2397-3366. DOI: 10.1038/s41550-018-0658-y. URL: http://dx.doi.org/10.1038/s41550-018-0658-y.

[12] G. Woan. *The GEO600 Gravitational Wave Detector – Pulsar Prospects.* 2002. arXiv: astro-ph/0210649 [astro-ph]. URL: https://arxiv.org/abs/astro-ph/0210649.

[13] C. S. Unnikrishnan. *LIGO-India: A Decadal Assessment on Its Scope, Relevance, Progress, and Future.* 2023. arXiv: 2301.07522 [astro-ph.IM]. URL: https://arxiv.org/abs/2301.07522.

[14] Joshua S Speagle. "dynesty: a dynamic nested sampling package for estimating Bayesian posteriors and evidences". In: *Monthly Notices of the Royal Astronomical Society* 493.3 (Feb. 2020), pp. 3132–3158. ISSN: 1365-2966. DOI: 10.1093/mnras/staa278. URL: http://dx.doi.org/10.1093/mnras/staa278.

[15] Max Pettini. *Introduction to Cosmology Lecture 5.* https://people.ast.cam.ac.uk/~pettini/Intro%20Cosmology/Lecture05.pdf. Lecture slides, University of Cambridge. 2018.

[16] N. Aghanim et al. "Planck2018 results: VI. Cosmological parameters". In: *Astronomy amp; Astrophysics* 641 (Sept. 2020), A6. ISSN: 1432-0746. DOI: 10.1051/0004-6361/201833910. URL: http://dx.doi.org/10.1051/0004-6361/201833910.

[17] Adam G. Riess et al. "Cosmic Distances Calibrated to 1% Precision with Gaia EDR3 Parallaxes and Hubble Space Telescope Photometry of 75 Milky Way Cepheids Confirm Tension with CDM". In: *The Astrophysical Journal Letters* 908.1 (Feb. 2021), p. L6. ISSN: 2041-8213. DOI: 10.3847/2041-8213/abdbaf. URL: http://dx.doi.org/10.3847/2041-8213/abdbaf.

[18] Kenneth C Wong et al. "H0LiCOW – XIII. A 2.4 per cent measurement of H0 from lensed quasars: 5.3 tension between early- and late-Universe probes". In: *Monthly Notices of the Royal Astronomical Society* 498.1 (Sept. 2019), pp. 1420–1439. ISSN: 1365-2966. DOI: 10.1093/mnras/stz3094. URL: http://dx.doi.org/10.1093/mnras/stz3094.